Ultramicroscopy 214 (2020) 113005

Contents lists available at ScienceDirect

Ultramicroscopy

journal homepage: www.elsevier.com/locate/ultramic

Achieving diffraction-limited resolution in soft-X-ray Fourier-transform holography

Jan Geilhufe[a], Bastian Pfau[a,*], Christian M. Günther[b,c], Michael Schneider[a], Stefan Eisebitt[a,b]

[a] Max Born Institute for Nonlinear Optics and Short Pulse Spectroscopy, Max-Born-Str. 2A, Berlin 12489, Germany
[b] Technische Universität Berlin, Institut für Optik und Atomare Physik, Straße des 17. Juni 135, Berlin 10623, Germany
[c] Technische Universität Berlin, Zentraleinrichtung Elektronenmikroskopie (ZELMI), Straße des 17. Juni 135, Berlin 10623, Germany

ARTICLE INFO

Keywords:
X-ray imaging
Holography
Resolution

ABSTRACT

The spatial resolution of microscopic images acquired via X-ray Fourier-transform holography is limited by the source size of the reference wave and by the numerical aperture of the detector. We analyze the interplay between both influences and show how they are matched in practice. We further identify, how high spatial frequencies translate to imaging artifacts in holographic reconstructions where mainly the reference beam limits the spatial resolution. As a solution, three methods are introduced based on numerical post-processing of the reconstruction. The methods comprise apodization of the hologram, refocusing via wave propagation, and deconvolution using the transfer function of the imaging system. In particular for the latter two, we demonstrate that image details smaller than the source size of the reference beam can be recovered up to the diffraction limit of the hologram. Our findings motivate the intentional application of a large reference-wave source enhancing the image contrast in applications with low photon numbers such as single-shot experiments at free-electron lasers or imaging at laboratory sources.

1. Introduction

X-ray Fourier-transform holography (FTH) is a coherent, lensless imaging method that offers high spatial resolution as well as high photon efficiency in conjunction with a simple and robust scattering setup [1]. Since the access to the sample is not hindered by any X-ray optics, FTH has great flexibility for the design of pump–probe experiments with state-of-the-art resolution in time and space. In the past years, these unique FTH features have mostly been utilized to study functional magnetic thin films [2–5] and nanostructures [6,7] by exploiting the X-ray magnetic circular dichroism as contrast mechanism. Time-resolved holography experiments have been demonstrated at 3rd-generation synchrotron-radiation sources [8,9], free-electron lasers (FEL) [10] and table-top EUV laser [11]. Even though magnetic thin films are currently the main application of FTH imaging, the method has recently been applied to study nanometer-scale phase-separation in a correlated material [12] and to image a free-flying virus [13].

In the most common implementation of FTH, the field of view (FOV) is defined by a micrometer-sized object aperture, integrated in an otherwise opaque metal film. The source of the phase-encoding reference beam is a small pinhole of few tens of nanometer in diameter laterally offset to the object aperture. By illuminating such an integrated mask with a coherent X-ray beam, the interference pattern between the beams transmitted through both apertures, which constitutes the hologram, can be recorded in the far field. The reconstruction of the complex wave field exiting the object is determined by a Fourier transform of the hologram returning the cross-correlation of the reference pinhole's exit wave and the object wave [1,14]. The image formation by the cross-correlation is the first limitation of the spatial resolution in an FTH experiment. In addition, the resolution of the reconstruction is limited by the maximum momentum transfer up to which the hologram can be recorded, be it due to finite detector size or signal-to-noise ratio being too small at high momentum transfer. In this work, we consider the first case, where the finite size of the detector acts as a low-pass filter for the hologram reconstruction. Regarding the geometric limitations, both the FTH system's angular resolution set by the detectors numerical aperture (NA) as well as the reference pinhole affect the spatial resolution and should ideally be matched for best overall performance of the imaging system.

Present-day X-ray area detectors enable large NAs due to their dimensions while reference pinholes provide only limited scattering angles due to their finite extend. Pinhole references, thus, represent a bottleneck in terms of real-space resolution. Apart from their influence on the spatial resolution, the size of the reference pinhole also affects

* Corresponding author.
E-mail address: bastian.pfau@mbi-berlin.de (B. Pfau).

https://doi.org/10.1016/j.ultramic.2020.113005
Received 9 October 2019; Received in revised form 27 February 2020; Accepted 19 April 2020
Available online 28 April 2020

the photon efficiency of the method, as the reference signal on the detector and ultimately the image contrast in the reconstruction will diminish for smaller and, thus, higher-resolution pinholes, ultimately leading to an imbalance between the intensity of the object and reference wave. The choice of the reference pinhole diameter is therefore merely a compromise that trades photon efficiency for spatial resolution. Experimental or numerical (i.e., post-experimental) solutions to improve the efficiency or resolution independently from each other will directly improve the method's productivity at synchrotron-radiation sources where FTH is already routinely applied. More importantly, new solutions are needed to increasingly apply FTH in femtosecond time-resolved experiments at high-harmonic generation sources [15–17] or single-shot experiments at FELs [10,18–20] where the number of available photons is limited in both cases.

A feasible way out of the dilemma is to manufacture an integrated mask with extended references such as pinhole arrays [21,22], Fresnel zone plates [23] or extended shapes with sharp edges (e.g., a slit or triangle) based on the so-called HERALDO principle [3,9,24]. Such approaches are especially promising to drastically boost the reference signal strength and, thus, the image contrast in the reconstruction, provided the reference beam intensity is limiting the hologram modulation at high momentum transfer. Much like pinhole references, however, the spatial resolution that can ideally be provided by extended references is still limited by manufacturability constraints and not by the maximum scattering angle recorded by the holography setup. In contrast to common, diffraction-limited imaging systems where features smaller than the diffraction limit are absent in the image, a strongly reference-limited hologram still contains high-resolution information but the standard reconstruction method fails to correctly reproduce the features associated with this information.

Previous attempts to recover this information are predominately based on iterative phase-retrieval algorithms. While these algorithms were initially developed to reconstruct a real-space image from the measured coherent diffraction pattern of the sample alone, a method referred to as coherent diffraction imaging (CDI) [25], the same procedure using the hologram as CDI input was employed for refinements of FTH reconstructions in proof-of-principle experiments [17,20,21,26,27]. Typically, the holographic information content in the data is hardly exploited in these attempts. Consequentially, CDI refinement suffers from the same limitations as CDI itself: First, if the sample is highly symmetric, CDI frequently fails to find a unique solution. Second, CDI is extremely sensitive to the input data quality. In particular, missing or deficient scattering information at low scattering angles severely hamper the convergence. As a result, previous test experiments have typically imaged artificial samples with a high degree of asymmetry, high (typically binary) contrast and a composition of primarily high spatial frequencies [20,21,26] which is in stark contrast to the situation found in many imaging applications, e.g., for materials science.

In this study, we discuss the limitation of pinhole references in large-NA setups in detail. In particular, we attribute imaging artifacts in the reconstruction to the scattering signal at large momentum transfer originating from object features that are smaller than the reference pinhole utilized. We propose design parameters for conventional FTH to match the reference size and the angular resolution of the scattering geometry in order to circumvent the artifacts discussed and to deliver an optimized reference signal. For strongly reference-limited holograms where the angular resolution of the scattering geometry is superior to the reference size, we demonstrate two post-experimental methods that allow translating the cause of the artifacts, i.e., the scattering signal at large momentum transfer, into an enhancement of the real-space resolution. The first method relies on free-space propagation [28,29] of the reconstruction and does not require any knowledge about the exact shape of the reference pinhole whereas the second method aims to characterize the reference source to enable a holographic reconstruction with potentially diffraction-limited resolution via deconvolution. Both numerical methods deliver unambiguous solutions, are straightforward to apply to the holography data and can, thus, be effectively integrated into online image reconstruction.

2. Theory

Considering transmission functions of a reference pinhole $p(\boldsymbol{r})$ as well as an arbitrary object $o(\boldsymbol{r})$ that are separated by the vector $\boldsymbol{r}_0$ in the mask plane, the hologram recorded by a detector in the far field over an area of $A_\mathrm{D}(\boldsymbol{q})$ can be described by the interference term:

$$H(\boldsymbol{q}) = A_\mathrm{D}(\boldsymbol{q})\,|\mathcal{F}[p(\boldsymbol{r}-\boldsymbol{r}_0)] + \mathcal{F}[o(\boldsymbol{r})]|^2 \tag{1}$$

$$\begin{aligned} = \; & A_\mathrm{D}(\boldsymbol{q})\{|\mathcal{F}[p(\boldsymbol{r})]|^2 + |\mathcal{F}[o(\boldsymbol{r})]|^2 \\ & + \mathcal{F}[p(\boldsymbol{r})]\mathcal{F}^*[o(\boldsymbol{r}-\boldsymbol{r}_0)] \\ & + \mathcal{F}[o(\boldsymbol{r}+\boldsymbol{r}_0)]\mathcal{F}^*[p(\boldsymbol{r})]\}, \end{aligned} \tag{2}$$

with $\boldsymbol{r}$ and $\boldsymbol{q}$ being real and reciprocal space coordinates, respectively, and $\mathcal{F}$ denoting the Fourier transform and $\mathcal{F}^*$ the complex conjugate of the Fourier transform.

The detector area $A_\mathrm{D}(\boldsymbol{q})$ can also be conceived as the imaging system's pupil function which in the simplest case is unity inside the boundaries of the sensitive detector area and zero outside [30]. Upon Fourier transforming the hologram $H(\boldsymbol{q})$, the first two intensity terms on the right side of the expanded Eq. (2) yield the central autocorrelation whereas the second two terms result in two redundant, conjugated cross-correlations, constituting the actual reconstruction, i.e., image of the exit wave leaving the object.

2.1. Point-spread function and transfer function

Only for infinitely large detectors, the real-space reconstruction would be given by the cross-correlation of the complex transmission functions of reference pinhole and the object. For experimentally recorded holograms, the actual point-spread function (PSF) of the FTH imaging system, however, depends on how the interference pattern is low-pass filtered by the detector area $A_\mathrm{D}(\boldsymbol{q})$, i.e., on the pupil function in the far field. The transfer of the object's spatial frequencies into the reconstruction depending on their wave vector $\boldsymbol{q}$ can be described by defining the transfer function (TF) of the FTH imaging system:

$$\mathrm{TF}(\boldsymbol{q}) = A_\mathrm{D}(\boldsymbol{q})\mathcal{F}[p(\boldsymbol{r})]. \tag{3}$$

The point-spread function (PSF) is then given by the Fourier transformation of the TF resulting in a convolution (*) of the reference pinhole shape and the Fourier transform of $A_\mathrm{D}(\boldsymbol{q})$:

$$\mathrm{PSF}(\boldsymbol{r}) = \mathcal{F}[\mathrm{TF}(\boldsymbol{q})] \tag{4}$$

$$= \mathcal{F}[A_\mathrm{D}(\boldsymbol{q})]*p(\boldsymbol{r}). \tag{5}$$

2.2. Circular reference wave source

In the common implementation of FTH, a circular aperture is employed as source of the reference wave. The far-field diffraction $\mathcal{F}[p(\boldsymbol{r})]$ from the aperture with diameter $d_\mathrm{ref} = 2r_\mathrm{ref}$ is given by Goodman [30]:

$$E_\mathrm{ref}(q) = E_0\frac{2J_1(qr_\mathrm{ref})}{qr_\mathrm{ref}}. \tag{6}$$

The wave field is isotropic and only depends on the magnitude of the wave vector ($q = |\boldsymbol{q}|$). J_1 denotes the Bessel function of first kind and E_0 is a scaling factor which describes the maximum field amplitude of the reference beam on the detector. For a given X-ray wavelength (λ) and distance of the detector to the specimen, the extent of $E_\mathrm{ref}(q)$ scales inversely with the radius of the reference pinhole while the detector area $A_\mathrm{D}(\boldsymbol{q})$ which restricts $\mathrm{TF}(\boldsymbol{q})$ remains constant. Different from most lens-based imaging systems, the transfer function of an FTH system using a large detector, thus, exhibits negative frequency bands (blue

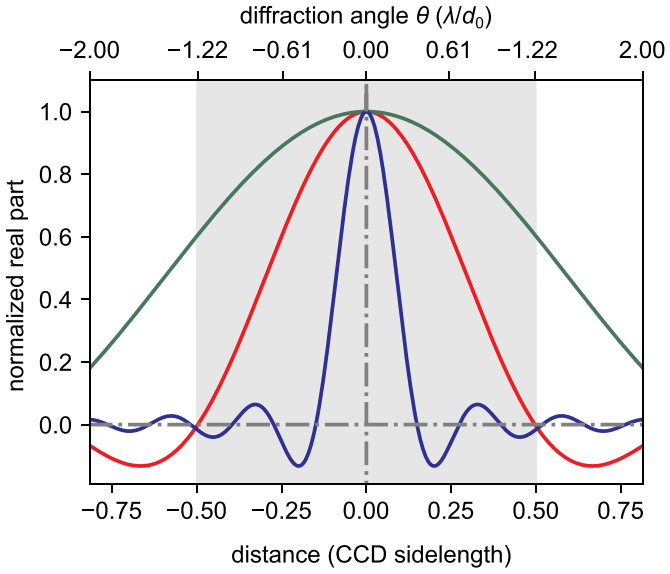

Fig. 1. Transfer function of a Fourier-transform holography imaging system. The plots show the far-field diffraction (real part) from a circular reference pinhole with three different diameters. The scattering is compared with the detector size indicated by the gray-shaded area. In the optimal case (), the first zero of the reference pinhole's diffraction matches the largest scattering angle that can be recorded by the detector (red). For scattering geometries with smaller reference size (here: $d_{\mathrm{ref}} = 0.5d_0$) and corresponding larger Airy disk, the reconstruction becomes increasingly detector limited (green). For scattering geometries that accommodate higher orders of the reference pinhole's diffraction on the detector (here: $d_{\mathrm{ref}} = 4d_0$), the reconstruction becomes more reference-limited (blue). Negative side lobes of the Bessel function are transferred into the reconstruction with reversed amplitude resulting in imaging artifacts in the reconstruction for corresponding spatial periods. (For interpretation of the references to color in this figure legend, the reader is referred to the web version of this article.)

curve in Fig. 1). Since the transfer function is generally unknown, frequencies outside the first zero-crossing cannot contribute to the spatial resolution of the reconstruction as these frequencies may or may not be reversed in amplitude. Common, diffraction-limited imaging systems have non-negative transfer functions and a defined cut-off frequency which excludes features below the resolution limit from the real-space image. On the contrary, the non-zero amplitudes of the transfer function beyond the first zero-crossing still transfer spatial information smaller than d_{ref} into the reconstruction [31]. The inversion of various spatial frequencies for structures smaller than d_{ref}, however, leads to an appearance of features in the reconstruction that do not resemble the actual specimen. In the following, we, thus, label these artificial features contrast-inversion artifacts and describe three methods to rectify this artifact. In particular the last method based on deconvolution also significantly improves the spatial resolution.

2.3. Low-pass filtering

A direct approach to circumvent contrast-inversion artifacts is to delete all spatial frequencies in the hologram that correspond to the negative side bands of the transfer function. This can easily be achieved by applying a circular low-pass filter with a radius that matches the first zero of the reference pinhole diffraction ($E_{\mathrm{ref}}(q)$) on the hologram recorded. The application of such a window function (so-called apodization) results in a non-negative transfer function that is given by the central (positive) part of the reference pinhole's diffraction and therefore smoothly suppresses the amplitudes of increasing spatial frequencies of the object. In addition to eliminating the contrast-inversion artifact, such a naturally apodized transfer function results in a reconstruction with suppressed edge ringing [30] and an image contrast that decreases strictly monotonic for higher spatial frequencies. The numerical aperture of this imaging system is simply given by the radius of the apodization window.

In order to optimally exploit the detector area, the FTH system's NA can be adjusted such that the first zero-crossing of $E_{\mathrm{ref}}(q)$, i.e., the size of the reference wave's Airy disk matches the boundaries of the detector area (red curve in Fig. 1). In order to account for commonly square-shaped detectors, matching the NA ideally also involves the application of a circular windowing as described above. We consider such a configuration an optimal trade-off between photon efficiency and spatial resolution. For a broader Airy disk (i.e., smaller reference diameter) with the first zero outside the boundaries of the detector, the transfer function becomes increasingly dominated by the shape of the detector ($A_{\mathrm{D}}(\boldsymbol{q})$ in Eq. (3)). In this case, the FTH system becomes increasingly *diffraction limited*, i.e., the resolution becomes increasingly independent from the reference hole diameter, but rather limited by the low-pass filtering of the detector (green curve in Fig. 1). Such a configuration is inefficient, as either the interference pattern is not captured up to the maximum scattering angles that potentially could contribute to the reconstruction given the small reference hole size or a larger reference hole could be used increasing the reference wave intensity. In contrast, FTH systems with an reference Airy disk narrower than the optimal configuration show a transfer function that does not utilize the information up to the maximum scattering angle recorded (blue curve in Fig. 1). Such holograms are overly *reference limited*. The usable part of such a hologram within the first zero of pinhole diffraction covers only a small part of the detector resulting in an inefficient use of the device. The situation improves by decreasing the FTH system's NA via placing the detector further downstream from the specimen. As a result, the scattering signal is distributed over a larger number of pixels and the detector's limited dynamic range is exploited more efficiently which finally leads to a better signal-to-noise ratio of the reconstructions.

2.4. Focusing by propagation

Another way to deal with negative side lobes of a transmission function which is strongly reference limited is to recover negative (high) spatial frequencies. Such an approach would ultimately also improve spatial resolution of the image reconstruction. The method presented here exploits the longitudinal shape of the point-spread function along the beam propagation axis (z). For a strongly reference-limited imaging system as considered here the PSF is dominated by the near-field diffraction from the reference pinhole. The natural reconstruction plane along z upon Fourier transforming the hologram is the plane of the object's exit wave from the integrated mask [1]. The PSF of a strongly reference-limited FTH system, however, approximates the transmission function of the reference pinhole, i.e., a circular disk, and neither coincides with the plane of maximum signal on-axis nor with the plane of least confusion at $d_{\mathrm{ref}}^2/4z\lambda = 1$ (Fig. 2). Defining $z = 0$ in the mask plane and assuming an infinitely thin mask, the PSF of a strongly reference-limited FTH system shows a real and a virtual beam waist which are symmetrically located upstream and downstream of the mask where the absolute value of the Fresnel number ($F = d_{\mathrm{ref}}^2/4z\lambda$) equals unity. The beam waists can, thus, be found at a propagation distances of $d_{\mathrm{prop}} = \pm d_{\mathrm{ref}}^2/4\lambda$. This is another fundamental difference to common, diffraction-limited imaging systems where the PSF after focusing is optimally confined in a single beam waist, i.e., in the imaging plane [31].

The PSF of a strongly reference-limited FTH system in the mask plane may, thus, be seen as a defocused image of a more confined PSF in the beam waist. Therefore, a direct approach to enhance the spatial resolution is to refocus the reconstruction by free-space propagation [29,30]. This operation is straightforward for a holographic reconstruction as both the amplitude and the phase information of the wave field are recovered. In fact, numerical free-space propagation was previously used to account for the distance between holographic mask

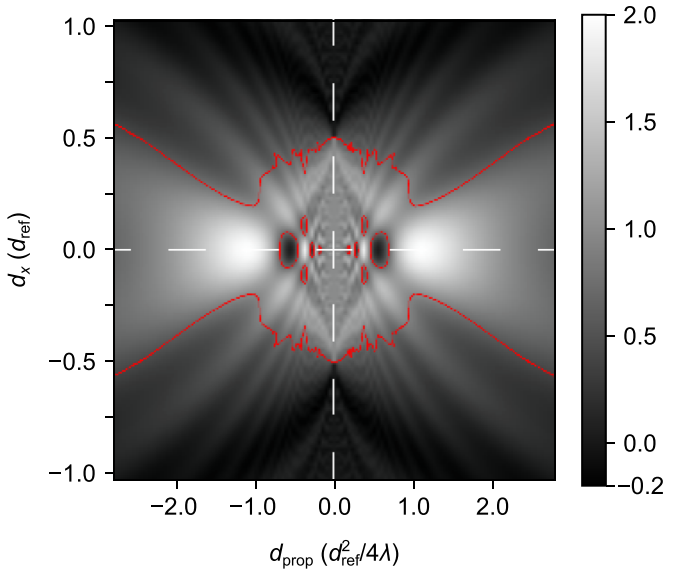

Fig. 2. Longitudinal shape of the PSF for a strongly reference-limited FTH system. For each distance d_{prop}, the PSF is normalized to the maximum at $d_{\mathrm{prop}} = 0$. The FWHM of the beam is indicated by red lines. (For interpretation of the references to color in this figure legend, the reader is referred to the web version of this article.)

and object in setups where mask and object were separated from each other [28,32,33]. To estimate the propagation distance to the beam waist, the reference pinhole may be regarded as a primitive, single-zone ($N = 1$) Fresnel zone plate (FZP). The distance from the mask plane to the beam waist positions can be interpreted as the FZP's first-order focal lengths:

$$f_{\mathrm{FZP}} = \frac{\pm 1}{N\lambda}(d_{\mathrm{ref}}/2)^2 = \frac{\pm d_{\mathrm{ref}}^2}{4\lambda}. \tag{7}$$

Refocusing the reconstruction leads, thus, to a resolution enhancement by a factor of up to two if the reference pinhole radius is interpreted as the outermost zone width of the single-zone FZP. The red line in Fig. 2 indicating the full width at half maximum (FWHM) of the reference beam clearly demonstrates the potential decrease in beam diameter at first-order focus. Similar to FZPs, the pinhole contains a zero order which can be removed by high-pass filtering the hologram [23,31]. This approach can push the resolution limit beyond the reference pinhole manufacturing capabilities and dispenses of the exact knowledge about the shape of the reference pinhole. However, the improvements of the resolution are limited by the diffraction efficiency of the reference pinhole's first diffraction order and by the superposition of higher orders [31].

2.5. Deconvolution

In order to use intentionally enlarged references with diameters much larger than the target resolution, we propose to characterize the transfer function in the mask-plane reconstruction to restore the resolution by a deconvolution method [14,34]. This approach aims to eliminate the reference-limiting term ($\mathcal{F}[p(\boldsymbol{r})]$) in TF($\boldsymbol{q}$) (Eq. (3)) and, thus, allows to exploit all spatial frequencies that where recorded over the whole detector area $A_{\mathrm{D}}(\boldsymbol{q})$ to reconstruct the object's wave field at diffraction-limited resolution. Due to the frequent zero-crossings of the transfer function of the coherent FTH imaging system, the application of a Wiener filter during deconvolution is mandatory [34]. Otherwise the deconvolution operator would diverge where TF($\boldsymbol{q}$) $\simeq 0$.

A one-dimensional illustration of the function of the deconvolution is shown in Fig. 3. The real part of the holographic transfer function approximated by Eq. (6) is shown in black. After applying the Wiener filter, the zero crossings are converted to singularities (purple). The deconvolution of the reconstruction is obtained by Fourier transforming the hologram after division by the Wiener-filtered transfer function. We note that wave propagation for resolution enhancement has a similar function as the deconvolution method. The relationship between both methods can be understood by comparing the transfer function to the normalized real part of the propagation operator that leads to an optimally focused reconstruction (blue). As seen by its sign, the operator also inverts negative side lobes of the transfer function, however, with some limitations. While the first order of the holographic transfer function is negated correctly, the propagation operator does not match the sign of the transfer function for diffraction angles $\theta > 2.9\lambda/d_{\mathrm{ref}}$ (marked by dashed line in Fig. 3). In other words, the propagation negates amplitudes that correspond to a positive side lobe of the transfer function. This results in an upper boundary for the resolution enhancement by a factor of $2.9/1.22 \simeq 2.4$. This figure is similar to the improvement by a factor of two predicted from the comparison of the reference aperture with an FZP.

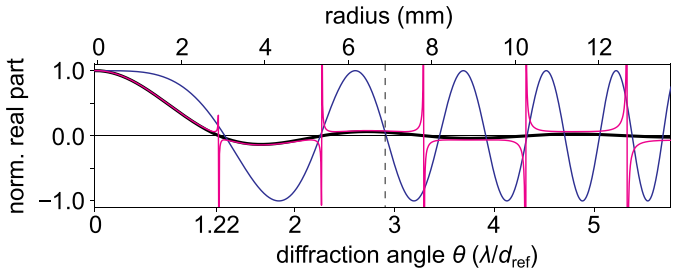

Fig. 3. One-dimensional illustration of the function of deconvolution and propagation. The normalized real part (radial average) of the approximated transfer function from the center of the diffraction pattern before (black), and after Wiener filtering (purple). The deconvolution is performed by dividing the recorded hologram by the Wiener filtered transfer function (purple). For comparison to the refocusing approach, the normalized real part of the free-space propagation that leads to an optimally focused reconstruction is given in blue. The amplitudes inverted by the wave propagation match only the first negative side lobe of the transfer function whereas amplitudes corresponding to diffraction angles $\theta > 2.9\lambda/d_{\mathrm{ref}}$ (dashed line) are not correctly negated by the refocusing approach. (For interpretation of the references to color in this figure legend, the reader is referred to the web version of this article.)

As the deconvolution approach relies on a sufficient knowledge of the system's transfer function, we here propose to characterize TF($\boldsymbol{q}$) by a reference test structure that is placed in the integrated mask next to the object taking advantage of a multiplexed FTH geometry [35]. The exit waves of the reference test structure and the desired object are both recorded simultaneously in a single measurement. Suitable reference test structures to analyze TF($\boldsymbol{q}$) are, for instance, sector stars. For a well-defined circular reference, TF($\boldsymbol{q}$) can sufficiently be approximated from the test structure reconstructed while performing deconvolutions with varying sizes of r_{ref} in Eq. (6) for the reference far-field $E_{\mathrm{ref}}(\boldsymbol{q})$. The appropriately scaled Bessel function is found when the deconvolution of the reference test structure is optimally reproduced, i.e., all sectors are optimally resolved with correct contrast for the sector star test structure.

3. Experiment

In a first experiment, all methods proposed above are investigated by imaging a sector-star test pattern with a strongly reference-limited FTH system. The test sample for this experiment consists of a silicon-nitride membrane, coated with a Cr/Au multilayer film on the facet-side rendering the structure opaque to soft X-rays. A field-of-view defining object hole with 5.25 μm in diameter was etched into the gold

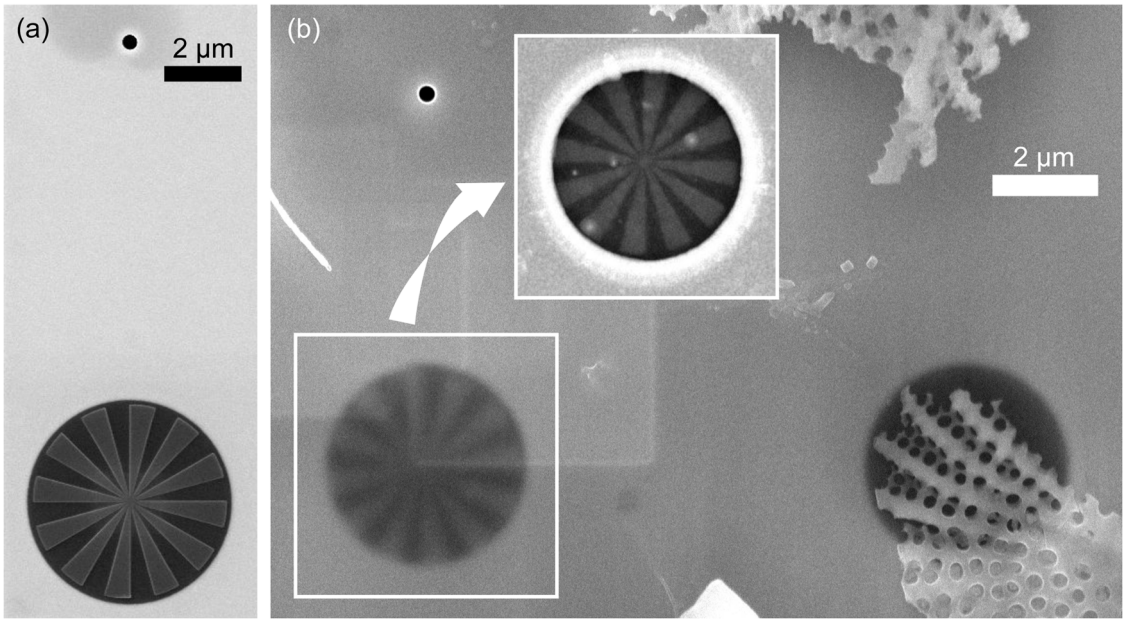

Fig. 4. Scanning electron micrographs (SEM) of test samples. (a) Sample to characterize a strongly reference-limited FTH transfer function using a sector star test pattern. (b) Sample to characterize a strongly reference-limited FTH transfer function to enhance the resolution of the reconstruction of a diatom test object. The sector star is seen by SEM through the silicon nitride membrane. The inset shows a SEM view from the opposite side.

layer using a focused-ion beam (FIB). The sector star which consists of 24 sectors and has a diameter of 5 µm was produced by electron-beam induced deposition of a 100 nm thick platinum layer at the object hole location. Note that this deposition method typically results in a high carbon content of the Pt layer of more than 80% [33]. The reference pinhole has a diameter of 350 nm and was milled from the mask side through all layers.

A second experiment aims to apply a characterized FTH transfer function to strongly reference-limited reconstruction of a natural test object. In this experiment, the substrate is again a silicon-nitride membrane, coated with a Cr/Au multilayer material for the FTH mask. Similar to the first sample, also this sample consists of a sector-star test pattern with 24 sectors. In addition to the sector star and the reference pinhole, the sample additionally contains a fossilized diatom shell as a natural object. To achieve this, diatomaceous earth was dispersed on the substrate and a suitable diatom shell was then selected by FIB milling of a 4µm wide object aperture into the mask on the opposite side of the membrane. Subsequently, the sector star (4 µm diameter) was produced in a second object aperture at a suitable location by electron-beam-assisted deposition of a 100 nm thick Pt layer. Note that the platinum was deposited on the membrane side opposite to the diatom (Fig. 4(b)). The reference pinhole with 300 nm in diameter was FIB milled through all layers.

The X-ray imaging experiments were carried out at the undulator beamlines U41-PGM and UE52-SGM of the synchrotron-radiation facility BESSY II (Berlin, Germany). The samples were illuminated by a coherent X-ray beam of 400 eV photon energy. The holograms were recorded by a CCD detector with 2048×2048 pixels and a square pixel shape with 13.5 µm side length which was placed 332 mm downstream the sample. In order to limit the dynamic range of the diffraction pattern, the central part of the CCD was masked by a circular beamstop to block the intense center of the hologram. For the second sample, the beam block was removed in a second exposure in order to also record the central part of the hologram. Subsequently both holograms where patched together matching the recorded signal in an overlap region. We recorded scattering signal up to the almost highest scattering angles covered by the detector. The potential diffraction-limited resolution for our detector geometry is 37 nm (half pitch).

The size of the pinholes providing the reference wave was intentionally chosen to be significantly larger than the achievable diffraction-limited resolution in order to operate in a strongly reference-limited regime. In this geometry, we are able to directly demonstrate the effects and methods discussed in the theory part above. Note that state-of-the-art FIB processing allows to routinely fabricate reference pinholes with diameters below 50 nm [4,5,7,12].

4. Results and discussion

Our analysis is based on the datasets as presented in Fig. 5. The hologram of the sector star comprises 30 CCD acquisitions where the intense central part is blanked out by a beamstop. The hologram of the diatom sample was assembled from 275 CCD acquisitions with beamstop and 1000 acquisition of the central area only without a beamstop. Afterwards the data was only corrected for the CCD background using CCD dark images and for intense cosmic-ray imprints by local thresholding. Nevertheless our data still suffers from (i) a spatially slowly varying background due to temporal drifts of the CCD noise (this was corrected for in the logarithmic display of the data in Fig. 5, but not in the image reconstruction), (ii) missing data behind the beamstop and the wire where it is attached to, (iii) transmission of high-energy radiation from undulator harmonics, and (iv) high CCD noise with respect to the signal level at high scattering angles. However, holographic imaging, picking up only the interference between object and reference waves, is very robust against such experimental shortcomings as we demonstrate in the reconstructions below. As a result, also the numerical image refinements presented here remain unaffected as they are based on the holographic reconstruction.

4.1. Reconstruction of the sector star

In Fig. 6, we show the reconstructions (real-part) of the sector star from the sample shown in Fig. 4(a) and the dataset in Fig. 5(a). We present the direct holographic reconstruction, i.e., the Fourier inversion of the hologram, in panel (a) and different post-treatments of it in panels (b)–(d). For each reconstruction, we calculate the image contrast in dependence on the feature size based on the intensity contrast between the sector-star spokes and the gaps in between. The contrast is azimuthally averaged over all spokes and normalized to the maximum

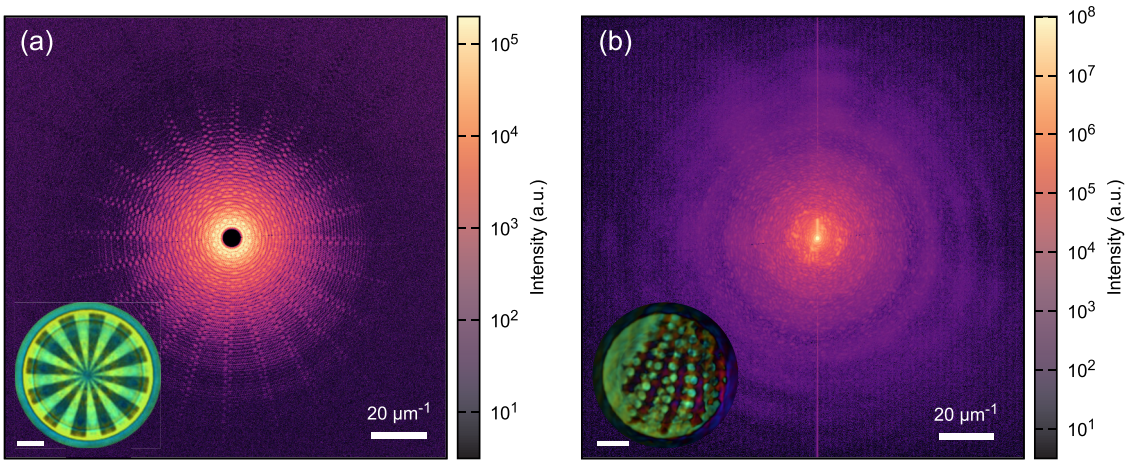

Fig. 5. Soft-X-ray holograms recorded from (a) the sector star sample and (b) the diatom sample. This data was used as basis for the entire analysis in this work. The holograms are displayed on a logarithmic intensity scale. For display only, a slowly varying background was additionally removed from the data in order to render the weak scattering at high scattering angles visible. While in (a) the central part of the hologram is blocked by a beamstop, the missing data in (b) was replaced using a second exposure without beamstop. The insets show the best reconstructions achieved from the holograms in a complex representation where value encodes magnitude and hue phase (for color representation see Fig. 7). Both reconstructions are based on a deconvolution of the initial FTH image. Reconstruction scalebars are 1 μm.

value, found at the rim of the sector star where the sectors are thoroughly modulated and the contrast ideally saturates. This mean contrast as a function of the sector width is given below the reconstructions. The error bars and the pale colored areas indicate the confidence interval for the contrast measurement according to the one-fold standard deviation. Note that this experimentally accessible contrast function is very similar, but not identical to the transfer function introduced in the theory part above (Eq. (3)). While the transmission function of our object is—in the ideal case—a rectangular function in the azimuthal direction, the transfer function would have to be directly probed by a Dirac-comb-like object. In order to evaluate the resolution limit achieved in a particular reconstruction, we define 15.3% image contrast as the resolution cut-off, similar to the Rayleigh criterion. The resolution limits determined are also indicated by the colored circles in the reconstructions.

The application of a central beamstop in the experiment results in strong high-pass filtering of the reconstructed image. As a consequence, information on spatially slowly varying features, in particular, the average transmission of the sample is lost. In our configuration, the cut-off corresponds to real-space distances of $\approx$ 1 μm and is, thus, still larger than the largest features found at the rim of the sector star. For this reason, the contrast functions in Fig. 6 are still unaffected by the beamstop. However, the Fourier inversion of the high-pass filtered data only yields the deviation of the transmission (given by the real part of the reconstruction) from its average. In particular, the filtering results in a real part with positive and negative values inside the FOV. Outside the FOV, where the radiation is blocked by the holography mask, the real part is still almost zero.

For the untreated reconstruction (Fig. 6(a)), the contrast decreases for smaller periods and vanishes for the spatial period that matches the reference pinhole diameter, i.e., we find the zero crossing at 178 nm half period in agreement with the nominal reference pinhole radius of 175 nm. Spatial periods between 101 nm and 178 nm appear to be contrast-inverted and the resolution limit for 15.3% image contrast is found for a feature width (half period) of 218 nm. The effective resolution in this geometry is, thus, clearly limited by the size of the

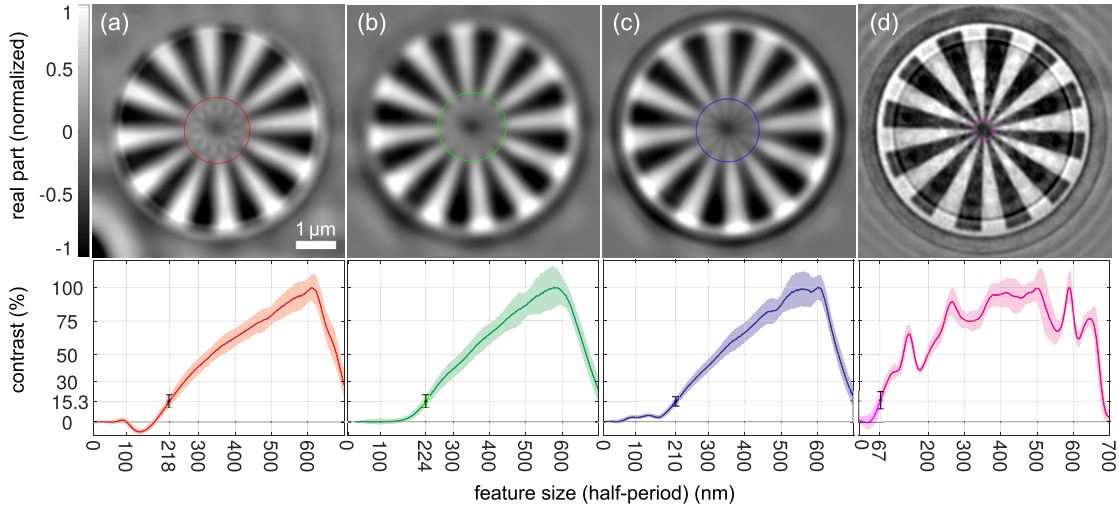

Fig. 6. Reconstruction of a sector star test pattern, (a) untreated reconstruction, (b) low-pass filtered reconstruction, (c) numerically refocused reconstruction (wave propagation), (d) reconstruction after deconvolution with an approximated FTH transfer function. The contrast in dependence on the spatial half period for each reconstruction is given below. The resolution cut-off is indicated for 15.3% image contrast. The confidence intervals according to the one-fold standard deviation of the contrast in the different sectors are indicated by error bars and by the pale-colored areas.

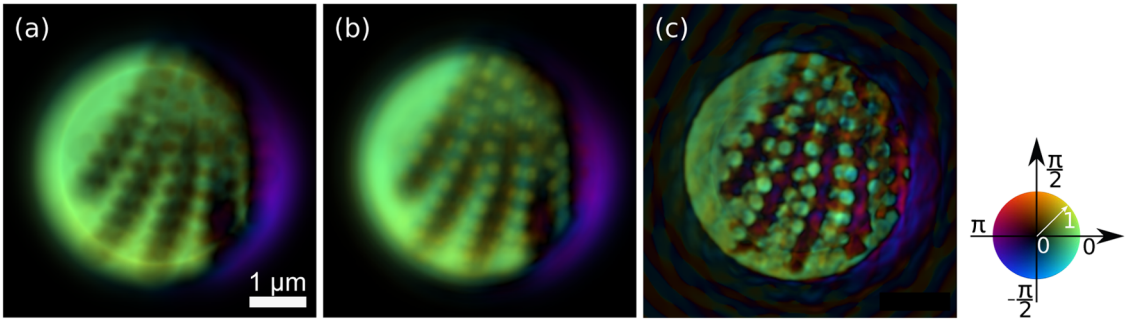

Fig. 7. Demonstration of resolution-enhanced imaging of a diatom as a natural test object (complex representation where value encodes amplitude and hue phase). (a) FTH reconstruction without further treatment. (b) Reconstruction after free-space propagation by 12 µm along the beam axis. (c) Reconstruction after deconvolution with Wiener filtering using a transfer function retrieved from a sector star imaged in parallel (not shown).

reference. We also find the imaging artifact from negative bands of the transmission function as predicted in our theory part above. In the following we will apply the numerical treatments suggested to cope with this artifact.

Fig. 6 (b) shows the reconstruction after applying a low-pass filter that deletes all frequencies outside the first zero crossing of the holographic transfer function TF($\boldsymbol{q}$). The inverse contrast artifact is now removed whereas the resolution is not significantly affected. Fig. 6(c) shows the reconstruction after propagation of the reconstructed object wave 12 µm along the beam axis, leading to an improvement of the contrast in the center of the sector star test pattern. The propagation distance is manually determined by bringing the smallest features into focus. The experimental propagation distance found is close to the nominal position of the first-order focus at 9.9 µm distance according to Eq. (7). We attribute the difference to wave-guide effects in the reference pinhole channel [17], which are neglected in our derivation of Eq. (7). After propagation, the center of the sector star is now correctly reproduced and the contrast inversion is resolved. After numeric refocusing, we achieve a resolution (half period) of 210 nm. This result is only marginally better than the resolution found for the low-pass filtered image. In particular, the experiment cannot confirm the improvement by a factor of two as predicted. This discrepancy finds its origin in the faint contrast of the reconstructed structures at half-pitch sizes of around 100 nm. As the propagation operator is always unity in Fourier space, it does not amplify these structures and their contrast remains below the threshold of 15.3% for the resolution cut-off. Nevertheless, the comparison between Fig. 6(a)–(c) clearly demonstrates that the numerically straightforward free-space propagation of the FTH reconstruction not only removes artifacts, but also unveils object details below the resolution threshold given by the reference wave source.

Fig. 6 (d) shows the sector star after Wiener deconvolution [30] using the approximated FTH transfer function. Assuming our reference pinhole has a circular shape, we found the best approximation of TF($\boldsymbol{q}$) as described above for a radius of the first zero equal to 2.97 mm on the detector. Considering our scattering geometry, this radius corresponds to a reference pinhole radius of 347 nm matching the nominal pinhole diameter of 350 nm from the manufacturing process remarkably well. After deconvolution, the sector star in the reconstruction is fully reproduced with high contrast over a wide band of spatial frequencies.

In order to reduce typical deconvolution artifacts caused by the sharp boundaries of the FOV [36], we smoothed the edge of the object pinhole in the reconstruction (Gaussian kernel with standard deviation 130 nm). While this procedure drastically reduces artifacts in the center of the FOV, the treatment sacrifices the outer region of the FOV. In the final reconstruction, we, therefore, replaced the rim area affected by smoothing with an image retrieved from a deconvolution process without any edge treatment. This method results in an inner region of the reconstruction that is free of boundary artifacts. The remaining boundary artifacts in the periphery of the FOV might be treatable with more sophisticated methods [36]. After deconvolution, the center of the sector star is clearly resolved. The image resolution even comes below the smallest features provided by the sector-star test structure. The resolution cut-off is found for feature sizes of 67 nm (half pitch) reaching almost diffraction-limited resolution and surpassing the resolution-limit achievable by wave-propagation method ($d_{\mathrm{ref}}/4 = 88$ nm (half pitch)). Since small spatial periods in the sector-star center strongly deviate from the ideal gap-to-period ratio of 0.5 (see Fig. 4(a)), the decrease in contrast for spatial half periods below 100 nm is not necessarily caused by the FTH imaging system, but the test sample. Consequentially, the resolution given is to be understood as an upper limit.

The optimized reconstruction from Fig. 6(d) is reproduced as an inset in Fig. 5(a) in a representation encoding both the magnitude as brightness and phase and hue. To realize this representation, an artificial offset was added to the reconstruction that compensates for the missing intensity blocked by the beamstop. This representation demonstrates that the sector star is also imaged in the phase of the reconstruction (phase difference between spokes and vacuum is ≈ 1 rad). However, the phase is subject to modulations again caused by the beamstop.

4.2. Reconstruction of the diatom sample

In Fig. 7, we show the reconstruction of the diatom object, again using different numerical treatments. Panel (a) shows the reconstruction of the diatom directly after Fourier inversion. The holes in the shell of the diatom are insufficiently resolved as they appear darker than the surrounding absorbing diatom. This finding again points to imaging artifacts because the hologram recorded is strongly reference limited. Fig. 7(b) shows the same reconstruction after numerically propagating the wave field by 12 µm. The transmission through the small holes is now reproduced correctly and the diatom appears more focused. In Fig. 7(c), we present the reconstruction after deconvolution using TF($\boldsymbol{q}$) approximated by Eq. (6). The numerical reference pinhole diameter as the only free deconvolution parameter was manually tuned utilizing the known sector star test pattern produced on the same sample and imaged simultaneously [35]. This tuning is as straight forward as adjusting a conventional focus. Typical deconvolution artifacts were treated similarly to the first experiment. Both the resolution and the contrast of the image improve significantly. The improvement reveals object details that have been hidden in the FTH reconstructions in (a) and (b). This demonstrates that information up to the diffraction limit can be extracted even from holograms recorded with a reference beam originating from an aperture which is much larger than this limit.

This finding directly leads to the idea of deliberately using a reference pinhole larger than the resolution intended for the experiment. This choice has two advantages: First, the more intense reference wave

coherently amplifies the scattering from the object which improves the signal against the detector's background noise. Second, a larger reference aperture can be produced with much better defined shape (e.g. circular) than apertures close to the resolution limit of the FIB and also X-ray wave-guiding effects are smaller for larger pinhole openings. This results in a better estimate for the reference exit wave which is utilized for the deconvolution. In addition, the combination of reference apertures with different diameters can be used to mutually fill the gaps in the contrast function originating from the zero-crossings of the transfer function.

While this study focuses on spherical pinholes as the most basic source for the reference wave, the theoretical and experimental findings can be transferred to extended reference objects, too. This is most straightforward for reconstructions from pinhole arrays which share the same properties as single-hole reconstructions. However, deconvolution approaches are also applicable to zone-plate-based holograms and the HERALDO method if a suitable estimate for the transfer function is used. Also in this case, the combination of the actual unknown object with well-defined test structures as proposed here is a promising way to directly evaluate the result in the experiment.

Recently, progress was reported also on numerical post-processing of holography data based on iterative phase-retrieval algorithms [17]. In this experiment imaging magnetic domains with extreme UV radiation, it is impressively demonstrated that high-contrast, diffraction-limited images can be obtained from reference-limited holograms if a high-quality, accurate and complete diffraction pattern is available. However such an input is experimentally challenging to achieve, in particular, with the presently available soft-X-ray detector technology having very limited dynamic range and typically low read-out speeds. Experiments with soft X-rays regime using similar samples could show no or only small improvements by the CDI refinement [24,27]. In particular, intentionally large reference apertures may even cause failing of the phase retrieval [27]. In contrast, the numerical methods presented here are also robust against missing information due to a central beamstop (Fig. 6(d)), high detector and photon noise at large scattering angles and contributions from higher harmonics of the fundamental wavelength which are typically present in undulator radiation. As our numerical methods are tuned by a single parameter (mainly reflecting the reference pinhole diameter), they can be easily integrated into instant image analysis.

5. Conclusion

In this work, we analyzed the interplay between detector size and the source size of the reference beam, which both can limit the spatial resolution achieved in an X-ray FTH experiment. We found that both effects should ideally be matched in a way that the Airy disk of the reference beam's far field exactly covers the area of the detector. If this geometry rule is experimentally followed and scattering signal with sufficient SNR is collected, diffraction-limited resolution of the FTH reconstructions can be expected.

In the main part of the work, we discussed the experimentally important case when the resolution is mainly limited by the reference beam while the diffraction limit would allow for better resolution. In this case, the hologram reconstruction shows significant imaging artifacts at small features due to negative side lobes of the FTH transfer function. We introduce three methods to circumvent these artifacts and improve the reconstructions. All methods rely on numerical post-processing of the reconstruction. We demonstrate that refocusing via wave-propagation as well as deconvolution are able to even retrieve spatial information beyond the limit given by the reference beam up to the diffraction limit. This result can even make the intentional application of reference pinholes larger than the spatial resolution required attractive. The use of large pinhole references allows enhancing the image contrast in the reconstruction for low photon number applications such as single-shot experiments at FELs [18,19] or imaging at laboratory sources [11,15–17]. In this case, the intensified reference wave coherently amplifies the object wave and, thus, increases the signal-to-noise ratio of the hologram and its reconstruction.

Funding information

The samples were manufactured at the TU Berlin Nano-Werkbank, which was supported by EFRE under contract number 20072013 2/22. Support by BMBF Verbundforschung (05K10KTB) is gratefully acknowledged.

Declaration of Competing Interest

The authors declare that they have no known competing financial interests or personal relationships that could have appeared to influence the work reported in this paper.

Supplementary material

Supplementary material associated with this article can be found, in the online version, at 10.1016/j.ultramic.2020.113005

References

[1] S. Eisebitt, J. Lüning, W.F. Schlotter, M. Lörgen, O. Hellwig, W. Eberhardt, J. Stöhr, Lensless imaging of magnetic nanostructures by X-ray spectro-holography, Nature 432 (7019) (2004) 885–888, https://doi.org/10.1038/nature03139. http://www.nature.com/doifinder/10.1038/nature03139

[2] C. Tieg, E. Jiménez, J. Camarero, J. Vogel, C. Arm, B. Rodmacq, E. Gautier, S. Auffret, B. Delaup, G. Gaudin, B. Dieny, R. Miranda, Imaging and quantifying perpendicular exchange biased systems by soft x-ray holography and spectroscopy, Appl. Phys. Lett. 96 (7) (2010) 072503, https://doi.org/10.1063/1.3291111. https://aip.scitation.org/doi/10.1063/1.3291111

[3] T.A. Duckworth, F.Y. Ogrin, G. Beutier, S.S. Dhesi, S.A. Cavill, S. Langridge, A. Whiteside, T. Moore, M. Dupraz, F. Yakhou, G.v.d. Laan, Holographic imaging of interlayer coupling in Co/Pt/NiFe, New J. Phys. 15 (2) (2013) 023045, https://doi.org/10.1088/1367-2630/15/2/023045. https://doi.org/10.1088/1367-2630/15/2/023045

[4] F. Büttner, I. Lemesh, M. Schneider, B. Pfau, C.M. Günther, P. Hessing, J. Geilhufe, L. Caretta, D. Engel, B. Krüger, J. Viefhaus, S. Eisebitt, G.S.D. Beach, Field-free deterministic ultrafast creation of magnetic skyrmions by spin orbit torques, Nat. Nanotechnol. 12 (11) (2017) 1040–1044, https://doi.org/10.1038/nnano.2017.178. http://www.nature.com/articles/nnano.2017.178

[5] L. Caretta, M. Mann, F. Büttner, K. Ueda, B. Pfau, C.M. Günther, P. Hessing, A. Churikova, C. Klose, M. Schneider, D. Engel, C. Marcus, D. Bono, K. Bagschik, S. Eisebitt, G.S.D. Beach, Fast current-driven domain walls and small skyrmions in a compensated ferrimagnet, Nat. Nanotechnol. 13 (12) (2018) 1154–1160, https://doi.org/10.1038/s41565-018-0255-3. http://www.nature.com/articles/s41565-018-0255-3

[6] S. Streit-Nierobisch, D. Stickler, C. Gutt, L.-M. Stadler, H. Stillrich, C. Menk, R. Frömter, C. Tieg, O. Leupold, H.P. Oepen, G. Grübel, Magnetic soft X-ray holography study of focused ion beam-patterned Co/Pt multilayers, J. Appl. Phys. 106 (8) (2009) 83909, https://doi.org/10.1063/1.3246724.

[7] B. Pfau, C.M. Günther, E. Guehrs, T. Hauet, T. Hennen, S. Eisebitt, O. Hellwig, Influence of stray fields on the switching-field distribution for bit-patterned media based on pre-patterned substrates, Appl. Phys. Lett. 105 (13) (2014) 132407, https://doi.org/10.1063/1.4896982. http://aip.scitation.org/doi/10.1063/1.4896982

[8] F. Büttner, C. Moutafis, M. Schneider, B. Krüger, C.M. Günther, J. Geilhufe, C. Schmising, J. Mohanty, B. Pfau, S. Schaffert, A. Bisig, M. Foerster, T. Schulz, C. Vaz, J.H. Franken, H.J.M. Swagten, M. Kläui, S. Eisebitt, Dynamics and inertia of skyrmionic spin structures, Nat. Phys. 11 (3) (2015) 225–228, https://doi.org/10.1038/nphys3234. http://www.nature.com/articles/nphys3234

[9] N. Bukin, C. McKeever, E. Burgos-Parra, P.S. Keatley, R.J. Hicken, F.Y. Ogrin, G. Beutier, M. Dupraz, H. Popescu, N. Jaouen, F. Yakhou-Harris, S.A. Cavill, G. van der Laan, Time-resolved imaging of magnetic vortex dynamics using holography with extended reference autocorrelation by linear differential operator, Sci. Rep. 6 (1) (2016) 1–10, https://doi.org/10.1038/srep36307. https://www.nature.com/articles/srep36307

[10] C. von Korff Schmising, B. Pfau, M. Schneider, C. Günther, M. Giovannella, J. Perron, B. Vodungbo, L. Müller, F. Capotondi, E. Pedersoli, N. Mahne, J. Lüning, S. Eisebitt, Imaging Ultrafast Demagnetization Dynamics after a Spatially Localized Optical Excitation, Phys. Rev. Lett. 112 (21) (2014), https://doi.org/10.1103/PhysRevLett.112.217203. https://link.aps.org/doi/10.1103/PhysRevLett.112.217203

[11] N.C. Monserud, E.B. Malm, P.W. Wachulak, V. Putkaradze, G. Balakrishnan, W. Chao, E. Anderson, D. Carlton, M.C. Marconi, Recording oscillations of sub-micron size cantilevers by extreme ultraviolet fourier transform holography, Opt.

Express 22 (4) (2014) 4161–4167, https://doi.org/10.1364/OE.22.004161. http://www.opticsexpress.org/abstract.cfm?URI=oe-22-4-4161

[12] L. Vidas, C.M. Günther, T.A. Miller, B. Pfau, D. Perez-Salinas, E. Martínez, M. Schneider, E. Gührs, P. Gargiani, M. Valvidares, R.E. Marvel, K.A. Hallman, R.F. Haglund, S. Eisebitt, S. Wall, Imaging nanometer phase coexistence at defects during the insulator metal phase transformation in VO_2 thin films by resonant soft X-ray holography, Nano Lett. 18 (6) (2018) 3449–3453, https://doi.org/10.1021/acs.nanolett.8b00458. http://pubs.acs.org/doi/10.1021/acs.nanolett.8b00458

[13] T. Gorkhover, A. Ulmer, K. Ferguson, M. Bucher, F.R.N.C. Maia, J. Bielecki, T. Ekeberg, M.F. Hantke, B.J. Daurer, C. Nettelblad, J. Andreasson, A. Barty, P. Bruza, S. Carron, D. Hasse, J. Krzywinski, D.S.D. Larsson, A. Morgan, K. Mühlig, M. Müller, K. Okamoto, A. Pietrini, D. Rupp, M. Sauppe, G. van der Schot, M. Seibert, J.A. Sellberg, M. Svenda, M. Swiggers, N. Timneanu, D. Westphal, G. Williams, A. Zani, H.N. Chapman, G. Faigel, T. Möller, J. Hajdu, C. Bostedt, Femtosecond X-ray Fourier holography imaging of free-flying nanoparticles, Nat. Photon. 12 (2018) 150–153, https://doi.org/10.1038/s41566-018-0110-y.

[14] B. Pfau, S. Eisebitt, X-Ray Holography, in: E. Jaeschke, S. Khan, J.R. Schneider, J.B. Hastings (Eds.), Synchrotron Light Sources and Free-Electron Lasers, Springer International Publishing, Cham, 2015, pp. 1–36, , https://doi.org/10.1007/978-3-319-04507-8_28-1. http://link.springer.com/10.1007/978-3-319-04507-8_28-1

[15] R.L. Sandberg, D.A. Raymondson, C. La-o vorakiat, A. Paul, K.S. Raines, J. Miao, M.M. Murnane, H.C. Kapteyn, W.F. Schlotter, Tabletop soft-x-ray Fourier transform holography with 50nm resolution, Opt. Lett., OL 34 (11) (2009) 1618–1620, https://doi.org/10.1364/OL.34.001618. https://www.osapublishing.org/ol/abstract.cfm?uri=ol-34-11-1618

[16] G.K. Tadesse, W. Eschen, R. Klas, V. Hilbert, D. Schelle, A. Nathanael, M. Zilk, M. Steinert, F. Schrempel, T. Pertsch, A. Tünnermann, J. Limpert, J. Rothhardt, High resolution XUV Fourier transform holography on a table top, Sci. Rep. 8 (1) (2018) 1–8, https://doi.org/10.1038/s41598-018-27030-y. https://www.nature.com/articles/s41598-018-27030-y

[17] O. Kfir, S. Zayko, C. Nolte, M. Sivis, M. Möller, B. Hebler, S.S.P.K. Arekapudi, D. Steil, S. Schäfer, M. Albrecht, O. Cohen, S. Mathias, C. Ropers, Nanoscale magnetic imaging using circularly polarized high-harmonic radiation, Sci. Adv. 3 (12) (2017), https://doi.org/10.1126/sciadv.aao4641. https://advances.sciencemag.org/content/3/12/eaao4641

[18] C.M. Günther, B. Pfau, R. Mitzner, B. Siemer, S. Roling, H. Zacharias, O. Kutz, I. Rudolph, D. Schondelmaier, R. Treusch, S. Eisebitt, Sequential femtosecond X-ray imaging, Nat. Photonics 5 (2) (2011) 99–102, https://doi.org/10.1038/nphoton.2010.287. https://www.nature.com/articles/nphoton.2010.287

[19] T. Wang, D. Zhu, B. Wu, C. Graves, S. Schaffert, T. Rander, L. Müller, B. Vodungbo, C. Baumier, D.P. Bernstein, B. Bräuer, V. Cros, S. de Jong, R. Delaunay, A. Fognini, R. Kukreja, S. Lee, V. López-Flores, J. Mohanty, B. Pfau, H. Popescu, M. Sacchi, A.B. Sardinha, F. Sirotti, P. Zeitoun, M. Messerschmidt, J.J. Turner, W.F. Schlotter, O. Hellwig, R. Mattana, N. Jaouen, F. Fortuna, Y. Acremann, C. Gutt, H.A. Dürr, E. Beaurepaire, C. Boeglin, S. Eisebitt, G. Grübel, J. Lüning, J. Stöhr, A.O. Scherz, Femtosecond single-shot imaging of nanoscale ferromagnetic order in Co/Pd multilayers using resonant X-Ray holography, Phys. Rev. Lett. 108 (26) (2012) 267403, https://doi.org/10.1103/PhysRevLett.108.267403. https://link.aps.org/doi/10.1103/PhysRevLett.108.267403

[20] F. Capotondi, E. Pedersoli, M. Kiskinova, A.V. Martin, M. Barthelmess, H.N. Chapman, A scheme for lensless X-ray microscopy combining coherent diffraction imaging and differential corner holography, Opt. Express, OE 20 (22) (2012) 25152–25160, https://doi.org/10.1364/OE.20.025152. https://www.osapublishing.org/oe/abstract.cfm?uri=oe-20-22-25152

[21] S. Marchesini, S. Boutet, A.E. Sakdinawat, M.J. Bogan, S. Bajt, A. Barty, H.N. Chapman, M. Frank, S.P. Hau-Riege, A. Szöke, C. Cui, D.A. Shapiro, M.R. Howells, J.C.H. Spence, J.W. Shaevitz, J.Y. Lee, J. Hajdu, M.M. Seibert, Massively parallel X-ray holography, Nat. Photonics 2 (9) (2008) 560–563, https://doi.org/10.1038/nphoton.2008.154. http://www.nature.com/articles/nphoton.2008.154

[22] C.M. Günther, E. Guehrs, M. Schneider, B. Pfau, C. von Korff Schmising, J. Geilhufe, S. Schaffert, S. Eisebitt, Experimental evaluation of signal-to-noise in spectro-holography via modified uniformly redundant arrays in the soft X-ray and extreme ultraviolet spectral regime, J. Opt. 19 (6) (2017) 64002, https://doi.org/10.1088/2040-8986/aa6380.

[23] J. Geilhufe, B. Pfau, M. Schneider, F. Büttner, C.M. Günther, S. Werner, S. Schaffert, E. Guehrs, S. Frömmel, M. Kläui, S. Eisebitt, Monolithic focused reference beam X-ray holography, Nat. Commun. 5 (1) (2014), https://doi.org/10.1038/ncomms4008. http://www.nature.com/articles/ncomms4008

[24] D. Zhu, M. Guizar-Sicairos, B. Wu, A. Scherz, Y. Acremann, T. Tyliszczak, P. Fischer, N. Friedenberger, K. Ollefs, M. Farle, J.R. Fienup, J. Stöhr, High-Resolution X-ray lensless imaging by differential holographic encoding, Phys. Rev. Lett. 105 (4) (2010) 043901, https://doi.org/10.1103/PhysRevLett.105.043901. https://link.aps.org/doi/10.1103/PhysRevLett.105.043901

[25] H.N. Chapman, K.A. Nugent, Coherent lensless X-ray imaging, Nat. Photonics 4 (12) (2010) 833–839, https://doi.org/10.1038/nphoton.2010.240. https://www.nature.com/articles/nphoton.2010.240

[26] L.-M. Stadler, C. Gutt, T. Autenrieth, O. Leupold, S. Rehbein, Y. Chushkin, G. Grübel, Hard Xray holographic diffraction imaging, Phys. Rev. Lett. 100 (24) (2008) 245503, https://doi.org/10.1103/PhysRevLett.100.245503. https://link.aps.org/doi/10.1103/PhysRevLett.100.245503

[27] S. Flewett, C.M. Günther, C.v.K. Schmising, B. Pfau, J. Mohanty, F. Büttner, M. Riemeier, M. Hantschmann, M. Kläui, S. Eisebitt, Holographically aided iterative phase retrieval, Opt. Express, OE 20 (28) (2012) 29210–29216, https://doi.org/10.1364/OE.20.029210. https://www.osapublishing.org/oe/abstract.cfm?uri=oe-20-28-29210

[28] E. Guehrs, C.M. Günther, B. Pfau, T. Rander, S. Schaffert, W.F. Schlotter, S. Eisebitt, Wavefield back-propagation in high-resolution X-ray holography with a movable field of view, Opt. Express 18 (18) (2010) 18922, https://doi.org/10.1364/OE.18.018922. https://www.osapublishing.org/oe/abstract.cfm?uri=oe-18-18-18922

[29] D.M. Paganin, Coherent X-ray Optics, Number 6 Oxford Series on Synchrotron Radiation, Oxford University Press, Oxford, 2013. OCLC: 841671941

[30] J.W. Goodman, Introduction to Fourier optics, third edition, Roberts & Company, Englewood, Colorado, 2005. OCLC: 249682655

[31] J. Geilhufe, High resolution soft X-ray Fourier transform holography, Technische Universität Berlin, 2015 Ph.D. thesis. https://depositonce.tu-berlin.de/handle/11303/4626

[32] D. Stickler, R. Frömter, H. Stillrich, C. Menk, C. Tieg, S. Streit-Nierobisch, M. Sprung, C. Gutt, L.-M. Stadler, O. Leupold, G. Grübel, H.P. Oepen, Soft x-ray holographic microscopy, Appl. Phys. Lett. 96 (4) (2010) 042501, https://doi.org/10.1063/1.3291942. https://aip.scitation.org/doi/abs/10.1063/1.3291942

[33] P. Hessing, B. Pfau, E. Guehrs, M. Schneider, L. Shemilt, J. Geilhufe, S. Eisebitt, Holography-guided ptychography with soft X-rays, Opt. Express 24 (2) (2016) 1840–1851, https://doi.org/10.1364/OE.24.001840. https://www.osapublishing.org/oe/abstract.cfm?uri=oe-24-2-1840

[34] H. He, U. Weierstall, J.C.H. Spence, M. Howells, H.A. Padmore, S. Marchesini, H.N. Chapman, Use of extended and prepared reference objects in experimental Fourier transform x-ray holography, Appl. Phys. Lett. 85 (13) (2004) 2454–2456, https://doi.org/10.1063/1.1795360. http://aip.scitation.org/doi/10.1063/1.1795360

[35] W.F. Schlotter, J. Lüning, R. Rick, K. Chen, A. Scherz, S. Eisebitt, C.M. Günther, W. Eberhardt, O. Hellwig, J. Stöhr, Extended field of view soft x-ray Fourier transform holography: toward imaging ultrafast evolution in a single shot, Opt. Lett. 32 (21) (2007) 3110, https://doi.org/10.1364/OL.32.003110. https://www.osapublishing.org/abstract.cfm?URI=ol-32-21-3110

[36] Renting Liu, Jiaya Jia, Reducing boundary artifacts in image deconvolution, 2008 15th IEEE International Conference on Image Processing, IEEE, San Diego, CA, USA, 2008, pp. 505–508, https://doi.org/10.1109/ICIP.2008.4711802. http://ieeexplore.ieee.org/document/4711802/